Understanding reliability and some limitations of the images and spectra reconstructed from a multi-monochromatic x-ray imager

T. Nagayama' , R. C. Mancini, D. Mayes, R. Tommasini, and R. Florido

Citation: Rev. Sci. Instrum. **86**, 113505 (2015); doi: 10.1063/1.4935828
View online: http://dx.doi.org/10.1063/1.4935828
View Table of Contents: http://aip.scitation.org/toc/rsi/86/11
Published by the American Institute of Physics

Understanding reliability and some limitations of the images and spectra reconstructed from a multi-monochromatic x-ray imager

T. Nagayama,[1,a)] R. C. Mancini,[1] D. Mayes,[1] R. Tommasini,[2] and R. Florido[3]
[1]*Physics Department, University of Nevada, Reno, Nevada 89557, USA*
[2]*Lawrence Livermore National Laboratory, Livermore, California 94550, USA*
[3]*Departamento de Física, Universidad de Las Palmas de Gran Canaria, 35017 Las Palmas de Gran Canaria, Spain*

(Received 5 June 2015; accepted 2 November 2015; published online 18 November 2015)

Temperature and density asymmetry diagnosis is critical to advance inertial confinement fusion (ICF) science. A multi-monochromatic x-ray imager (MMI) is an attractive diagnostic for this purpose. The MMI records the spectral signature from an ICF implosion core with time resolution, 2-D space resolution, and spectral resolution. While narrow-band images and 2-D space-resolved spectra from the MMI data constrain temperature and density spatial structure of the core, the accuracy of the images and spectra depends not only on the quality of the MMI data but also on the reliability of the post-processing tools. Here, we synthetically quantify the accuracy of images and spectra reconstructed from MMI data. Errors in the reconstructed images are less than a few percent when the space-resolution effect is applied to the modeled images. The errors in the reconstructed 2-D space-resolved spectra are also less than a few percent except those for the peripheral regions. Spectra reconstructed for the peripheral regions have slightly but systematically lower intensities by ~6% due to the instrumental spatial-resolution effects. However, this does not alter the relative line ratios and widths and thus does not affect the temperature and density diagnostics. We also investigate the impact of the pinhole size variation on the extracted images and spectra. A 10% pinhole size variation could introduce spatial bias to the images and spectra of ~10%. A correction algorithm is developed, and it successfully reduces the errors to a few percent. It is desirable to perform similar synthetic investigations to fully understand the reliability and limitations of each MMI application. [http://dx.doi.org/10.1063/1.4935828]

I. INTRODUCTION

Inertial confinement fusion (ICF) is a concept for an alternative energy source, which releases energy by compressing a millimeter-scale capsule containing fusion fuel (i.e., hydrogen isotopes such as tritium, T, and deuterium, D) with ablation pressure driven by mega-joule lasers.[1,2] Substantial progress has been made in theory, experiment, and diagnostics of ICF. However, efficient fuel burn, or *ignition*, has not yet been achieved, and discrepancies between experiments and simulations still remain.[3] While sources of discrepancies are extensively investigated,[4] diagnostics that directly reveal the evolution of the ICF implosion-plasma spatial structure are desired to advance ICF science towards ignition.

Multi-monochromatic x-ray imagers (MMIs) are attractive instruments for this purpose. The MMI is a unique 2-D spectrometer consisting of a pinhole array, a multilayered mirror (MLM), and a microchannel plate detector (MCP).[5,6] It records an array of ICF implosion-core images, each of which is formed by photons of slightly different energy. By processing MMI data, one can extract narrow-band images (i.e., intensity images of a narrow spectral range), space-integrated spectra,[7–9] and 2-D space-resolved spectra.[10] Spectroscopic analysis of MMI data provides a variety of approaches to constrain ICF plasma spatial structure in electron temperature, T_e, and electron density, n_e.

For example, we mixed a small fraction of Ar into D_2 gas fuel and analyzed Ar line emission to characterize T_e and n_e of the core. Using two narrow-band images, we inferred time-resolved 2-D T_e maps,[11] and from a collection of space-resolved spectra, we extracted n_e as well as T_e maps.[10] Synthetic investigations also suggest that time-resolved 3-D T_e and n_e spatial structure of ICF implosion cores can be studied by simultaneously analyzing collections of 2-D space-resolved spectra extracted from three MMI instruments fielded along quasi-orthogonal lines of sight.[12] Thus, MMI diagnostics have the potential to better constrain ICF experiments and advance ICF theory.

MMI processing consists of two parts: (1) basic processing and (2) post-processing.[9,10] The basic processing consists of optical-density to intensity conversion and a series of efficiency corrections associated with mirror reflectivity, filter transmission, flat-fielding, and MCP pore-angle dependent quantum efficiency. The post-processing is the process required to extract narrow-band images and space-resolved spectra after the basic processing has been applied. Because post-processing is numerically more involved, it is often mistaken to be the major source of the analysis inaccuracy. However, this post-processing part is quite reliable as long as it satisfies the reliability criterion discussed in Ref. 13.

[a)]Present address: Sandia National Laboratories, Albuquerque, New Mexico 87185-1106, USA.

In this article, we quantify the level of inaccuracy introduced into the reconstructed images and spectra due to the post-processing. The case of investigation is its application to the Ar-doped D_2 ICF implosion experiments. Specifically, we perform synthetic investigations for the spatial- and spectral-resolution effects. These effects are not obvious because resolution affects the MMI data first and then are propagated to the reconstructed images and spectra through the post-processing discussed in Refs. 9 and 10. In principle, images and spectra could be affected both by spatial resolution and spectral resolution.

We found that the reconstructed images are accurate within a few-percent error as long as a point-spread function is applied to the modeled image. The spectral-resolution effects on the image are negligible for our application because the line images are integrated over their spectral line width, which is much broader than the spectral resolution of the instrument.

Extracted space-resolved spectra are accurate within a few-percent error for the central region of the image as long as spectral-resolution effects are applied on the modeled space-resolved spectra. Spectra extracted from the periphery show an average absolute error of ~6%–7%. The larger discrepancies originate from the systematic intensity drop due to spatial convolution over the image boundary and from periodic artifacts due to the rapid intensity drop at the periphery. Since the intensity drop is systematic and the periodic artifacts oscillate about the expected value, their effects on the line ratio and width are much smaller. The T_e and n_e inferred from those spectra are accurate within a few-percent error.

We also investigated individual pinhole size variation and its effect on the images and spectra. This can introduce artificial spatial bias of ~10%. We developed a technique to correct the pinhole size-variation effects on the MMI data. The correction successfully removes the spatial bias and suppresses the errors to within a few percent.

The article is organized as follows. Sec. II describes the spectral model used to create synthetic MMI data and also to compute expected images and spectra. In Sec. III, we quantitatively investigate the spatial-resolution and spectral-resolution effects. Sec. IV describes pinhole size-variation effects on the extracted images and spectra, as well as their correction. Sec. V provides discussion and summary.

II. SPECTRAL MODEL

A. Emergent spectra as a function of (x, y) on the image plane

Our spectral model computes emergent spectra at every point on the image plane, $I_\nu(x, y)$, and then $I_\nu(x, y)$ is used to compute both synthetic MMI data and expected images and spectra. The case of investigation is an OMEGA direct-drive Ar-doped D_2 ICF implosion.[10,11] First, local emissivity and opacity of Ar are computed for ranges of T_e and n_e, and then, the emergent spectra, $I_\nu(x, y)$, are computed by solving the radiation transport along each chord, z, parallel to the line of sight.[12]

To compute the Ar emissivity, ϵ_ν, and opacity, κ_ν, necessary atomic data are computed by Flexible Atomic Code (FAC),[14] and Ar level populations are solved for grids of T_e and n_e with a collisional-radiative model, ABAKO.[15] We used the Stewart and Pyatt model[16] for continuum-lowering effects and the escape factor of a sphere to account for photo-pumping effects on the populations.[17] Spectral emissivity and opacity are computed from the calculated populations taking into account detailed Stark line profiles computed by MERL.[18]

Emergent spectra, $I_\nu(x, y)$ [erg/s cm^{-2} sr^{-1} eV^{-1}], are computed by numerically integrating the following radiation transport equation along chords in the source assuming parallel ray tracing,[19]

$$\frac{dI_\nu(x, y, z)}{dz} = \epsilon_\nu(x, y, z) - I_\nu(x, y, z)\,\kappa_\nu(x, y, z). \quad (1)$$

If (x, y, z) is inside the object, the quantities $\epsilon_\nu(x, y, z)$ and $\kappa_\nu(x, y, z)$ are determined at the given T_e and n_e using ABAKO. If (x, y, z) is outside the object, both $\epsilon_\nu(x, y, z)$ and $\kappa_\nu(x, y, z)$ are zero.

Theoretical uncertainty in the calculated emissivity and opacity does not affect the conclusions derived from our synthetic investigations because $I_\nu(x, y)$ is used to calculate both synthetic MMI data and expected images and spectra. What we pursue is an understanding of the discrepancies due to the processing of MMI data, whose spatial- and spectral-samplings are somewhat limited.

B. Expected images and spectra

Expected narrow-band images are computed by integrating $I_\nu(x, y)$ over any given spectral range as

$$I_{\Delta\nu}(x, y) = \int_{\Delta\nu} I_\nu(x, y)\, d\nu, \quad (2)$$

where $\Delta\nu$ is the bandwidth of interest.

Space-resolved spectra are computed by integrating $I_\nu(x, y)$ over any given spatial region of interest

$$I_{\nu,\Delta A} = \int_{\Delta A} I_\nu(x, y)\, da, \quad (3)$$

where ΔA is an arbitrarily shaped area of interest.

There are two different ways to deal with the instrumental-resolution effects. One is to deconvolve the resolution effects from the data. The other is to convolve resolution effects into the modeled images and spectra. We use the latter option because it is more straightforward and robust. For example, we can apply a 2-D Gaussian point-spread function to the expected images to account for instrumental spatial-resolution effects. Also, a 1-D Gaussian spectral profile can be applied to the expected spectra that account for instrumental spectral-resolution effects on the spectra.

C. Synthetic MMI data

Fig. 1(a) shows example MMI data. The detector plane is packed with a hexagonal array of pinhole implosion-core images. Due to the reflection of the MLM, each column of the MMI data picks out signals of specific photon energy, and the horizontal axis is also the spectral resolution axis.

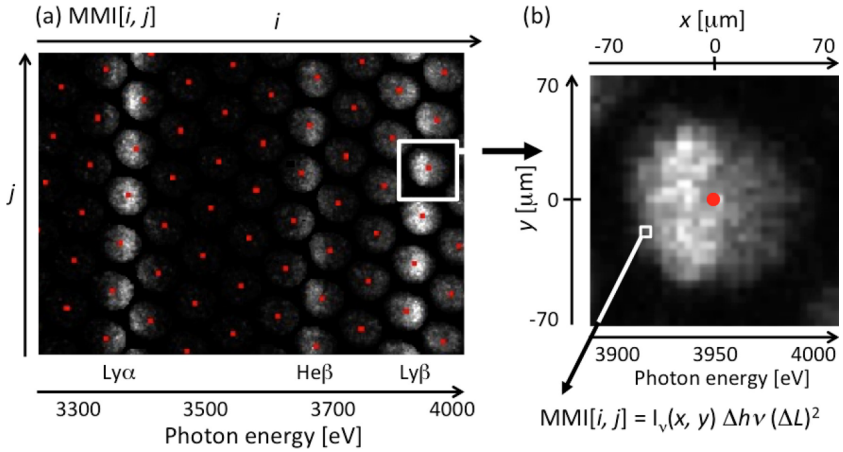

FIG. 1. (a) MMI data after efficiency correction. i and j are the horizontal and vertical indices of the pixels, respectively. The horizontal axis is also photon energy due to the spectral dispersion by the MLM. Red dots mark the pinhole-image centers. (b) Blow-up of one pinhole image. Each image has its own local spatial coordinates of the implosion core, (x, y). Each pixel value is proportional to $I_\nu(x, y)\Delta h\nu(\Delta L)^2$.

Fig. 1(b) is a blow-up of one pinhole image. After correcting for magnification, each pinhole image has its own local spatial coordinate of the implosion core, (x, y).

Thus, each pixel of the MMI data, MMI$[i, j]$, represents signal at a local position of the implosion core surface, $(x \pm \Delta L/2, y \pm \Delta L/2)$, of a very small spectral range, $h\nu \pm \Delta h\nu/2$. To model MMI data, the value of each pixel, MMI$[i, j]$, is computed as $I_\nu(x, y)\Delta h\nu(\Delta L)^2$, where $\Delta h\nu$ and ΔL are the spectral and spatial width of the pixel, $[i, j]$ (i.e., not the resolution of the instrument). The mapping from the MMI pixel $[i, j]$ to the corresponding point in the object space, (x, y), and the corresponding photon energy, $h\nu$, are different for every dataset and determined through the processing described in Ref. 9. Synthetic investigation becomes more useful when the mapping information comes from the actual data of interest.

Then, the spatial- and spectral-resolution effects are applied on the synthetic MMI data. Spatial resolution due to the pinholes is applied by convolving a 2-D Gaussian point-spread function of a spatial resolution given by pinhole size. Spectral-resolution effects are applied by convolving the synthetic MMI data with a Gaussian profile of a given resolution power along the horizontal direction.

The model also has an option to simulate pinhole size-variation effects due to an individual pinhole tolerance. When each pixel has the same pinhole size, the following 2-D Gaussian convolution is used to account for the spatial resolution effect:

$$MMI^{conv}[i, j] = A^{-1}\sum_{i'j'}\left[MMI[i', j'] \times \exp\left\{-\frac{(i'-i)^2+(j'-j)^2}{2\sigma_p^2}\right\}\right], \quad (4)$$

$$A = \sum_{i'j'}\exp\left\{-\frac{(i'-i)^2+(j'-j)^2}{2\sigma_p^2}\right\},$$

$$\sigma_p = D_p\frac{M+1}{M}\frac{1}{2\sqrt{2\ln 2}}\frac{1}{\Delta L},$$

where A^{-1} is the normalization constant and σ_p is the Gaussian convolution width. D_p is the pinhole diameter, a factor $(M+1)/M$ converts D_p to the full-width of the convolving area on the object, a factor $1/2\sqrt{2\ln 2}$ converts the full-width to the Gaussian width, and $1/\Delta L$ converts the units of the width to pixels. In reality, each pinhole has slightly different size than the nominal size D_{PH} due to the fabrication tolerance ΔD_{PH}. This produces variations in both brightness and convolving width of each pinhole image of the MMI data, which are numerically treated as follows.

1. Assign different pinhole size, D_p, to each pinhole, p, using a Gaussian random number generator based on a given nominal pinhole diameter, D_{PH}, and its tolerance, ΔD_{PH}.
2. For a given pixel $[i, j]$ of the synthetic MMI data,
   (a) find the pinhole p to which this pixel belongs and find its assigned diameter, D_p;
   (b) compute the convolution with a modified 2-D Gaussian using the assigned D_p,

$$MMI^{conv}[i, j] = B(D_p)A^{-1}\sum_{i'j'}\left[MMI[i', j'] \times \exp\left\{-\frac{(i'-i)^2+(j'-j)^2}{2\sigma_p^2}\right\}\right], \quad (5)$$

where D_p is the diameter of the pinhole to which this pixel belongs, σ_p is the Gaussian width for this particular pinhole, and $B(D_p) = D_p^2/D_{PH}^2$ is the simulated relative brightness with respect to the nominal. This simulates the effects of pinhole size variation in brightness and in spatial resolution. The pinhole shape is assumed to be circular, and the effect of the pinhole shape variation is neglected throughout this article.

III. QUANTITATIVE INVESTIGATIONS OF SPATIAL AND SPECTRAL RESOLUTION EFFECTS

The accuracy of the narrow-band images and spectra reconstructed from MMI data are quantitatively investigated using synthetic MMI data. We create synthetic MMI data that satisfy the criterion discussed in Ref. 13. We assume a 100-μm-diameter spherical plasma of uniform conditions

(T_e = 1500 eV and $n_e = 1.5 \times 10^{24}$ cm^{-3}). These values are characteristic values for the OMEGA direct-drive Ar-doped ICF implosion experiments reported previously.[10,11] The pinhole-array design and photon-energy axis used for the synthetic MMI data are those from the data shown in Ref. 11 that satisfy the criterion.

Then, we apply two different levels of instrumental details by following the technique discussed in Sec. II C. The first case, denoted as "ΔE," takes into account spectral resolving power of $E/\Delta E = 150$. The second case denoted as "ΔE, Δx," takes into account both the spectral resolution and the spatial resolution ($\Delta x = 11$ μm). These are typical values for the MLM and pinhole arrays used in our applications.

The images and spectra are reconstructed from these synthetic MMI data[9,10] and compared with the expected images and spectra computed as in Sec. II B. Comparisons of the images and spectra are discussed in Sec. III A and in Sec. III B, respectively.

A. Accuracy of reconstructed images

Fig. 2 compares Ar He-β images reconstructed from synthetic MMI data for cases (a) "ΔE" and (b) "ΔE, Δx" with (c) the expected He-β image. The reconstructed images for both cases agree with the expected image quite well. However, they show small artificial structures along the y direction, which correspond to the vertical direction in the MMI image and originate from the discrete nature of MMI data. These artifacts of a few percent in value are unavoidable and are limitations of the current MMI data and their processing technique.

The reconstructed image from the MMI data without spatial-resolution effects [i.e., Fig. 2(a)] best agrees with the expected images with an average absolute error of 1.5%. When the spatial-resolution effects are applied to the synthetic MMI data, the average absolute error increases to 7.1%.

Figs. 3(a) and 3(b) show percent-error surface plots computed for "ΔE" and "ΔE, Δx" with respect to the expected image, 2(c). While Fig. 3(a) reveals that the main source of error is from the observed vertical artifacts, the errors in (b) are largest at the image periphery. These large errors at the periphery are produced because the expected image shown 2(c) does not take into account spatial-resolution effects.

Next, we apply the 2-D Gaussian point-spread function of FWHM = 11 μm directly to the expected image and re-compute the error image for the case of "ΔE, Δx" to see if such an image is a more appropriate representation of the reconstructed images. We note that this treatment does not necessarily compensate for the spatial-resolution effects on the reconstructed images. This is because they are produced by applying the point-spread function and spectral-resolution effects directly to the MMI data, and then the effects are propagated through the processing. Fig. 3(c) shows the resultant percent-error image. The deep negative errors at the periphery disappear, and the percent error is dominated by the vertical artifacts as in the case of Fig. 3(a). The percent error is reduced from 7.1% to 1.4%.

To summarize, the image reconstruction is reliable with a few-percent error as long as the spatial-resolution effects are taken into account on the expected image. On one hand, the spectral-resolution effects on the reconstructed image are negligible for the applications presented here because the narrow-band images are computed by integrating a

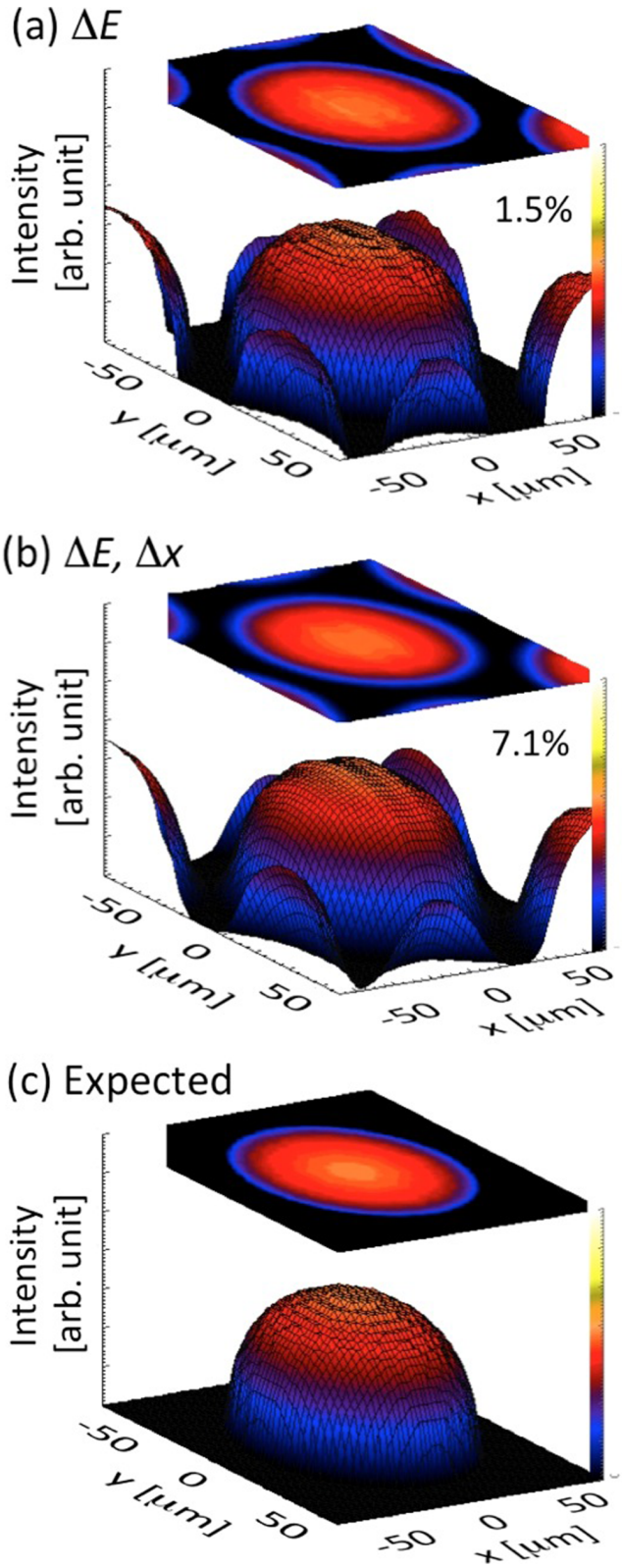

FIG. 2. Ar He-β images reconstructed from synthetic MMI data with (a) spectral resolution ($E/\Delta E = 150$), and (b) both spectral and spatial resolutions ($\Delta x = 11$ μm). (c) Expected image computed directly from the spectral model.

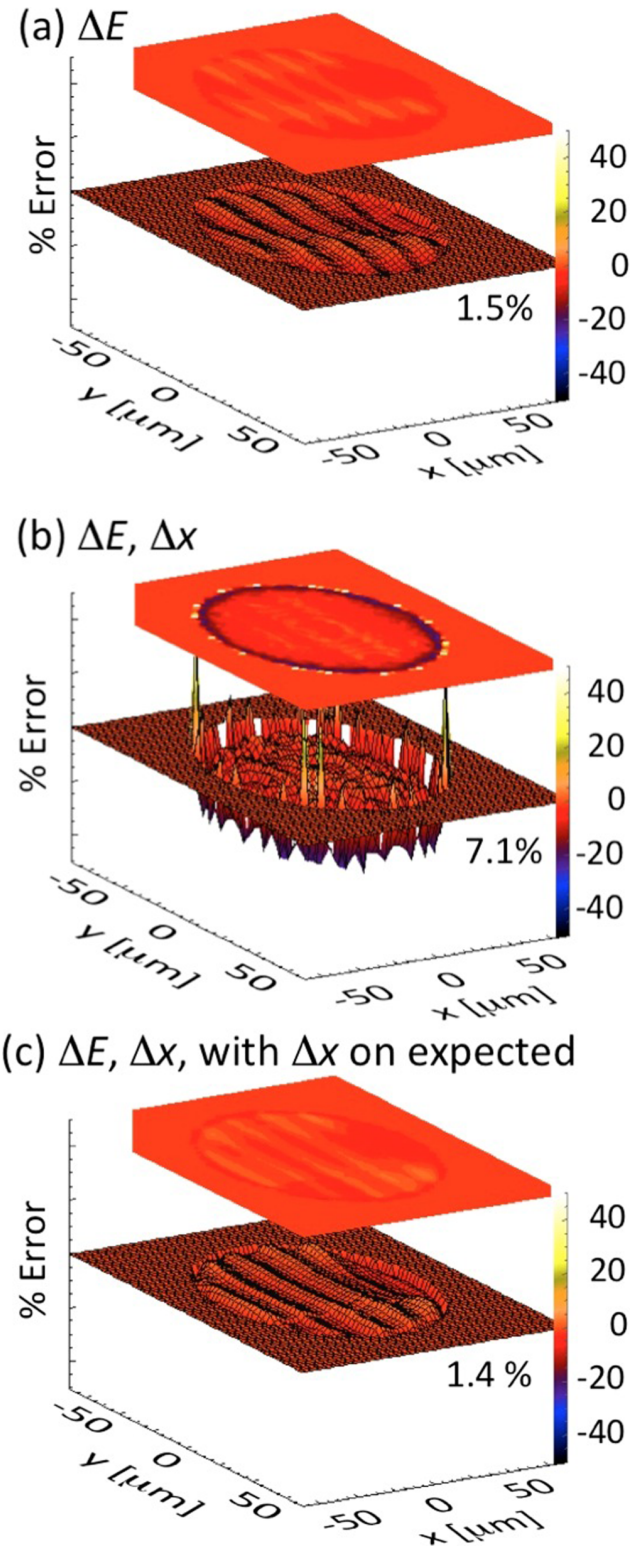

FIG. 3. Percent-error surface plots for He-β reconstructed from synthetic MMI data (a) with spectral resolution only and (b) with both spectral and spatial resolutions. The given percentages are averages of the absolute percent errors within the image regions. (c) is the same as (b) except that spatial-resolution effects are directly applied to the expected image used in the percent-error calculation.

monochromatic image over its spectral line width (i.e., $\Delta E \sim$ 60 eV) as in Eq. (2), which is significantly broader than the spectral resolution of the instruments. On the other hand, the spatial-resolution effects are not negligible and mostly affect the image periphery. The intensities at the image periphery are lowered because the convolving area partially exceeds the object boundary. Small vertical errors observed in Figs. 3(a) and 3(c) originate from the subtle vertical artifacts observed in Fig. 3, which are produced by the discrete nature of the MMI data.

B. Accuracy of reconstructed spectra

Space-resolved spectra are reconstructed from the synthetic MMI data with the technique discussed in Ref. 10. Spatial regions defined for the space-resolved spectra are shown in Fig. 4(a). Each spatial region can be categorized as belonging to the (b) central region, (c) top/bottom periphery, and (d) left/right periphery as shown in Fig. 4. These categories are important for understanding different sources of errors in MMI spectra. From the particular synthetic MMI data, 53 spatial regions are automatically defined using a minimum binning width comparable to the spatial resolution, ~11 μm. In this section, one spectrum is selected from each category (i.e., regions 30, 3, and 26, respectively) to discuss the source of error, and the rest are discussed through the average percent errors for central and peripheral regions.

Fig. 5(a) compares the reconstructed space-resolved spectra and the expected spectra for a central region [i.e., region 30 of Fig. 4(a)]. The solid red and dashed green lines are those reconstructed from synthetic MMI computed with "ΔE" and "ΔE, Δx" resolution options, respectively. They agree very well with the expected spectrum (i.e., dotted black). The average percent errors for "ΔE" and "ΔE, Δx" are 0.8% and 0.2%, respectively.

Fig. 5(b) shows similar comparisons for a top/bottom-periphery region (i.e., region 3 of Fig. 4). While they still show reasonable agreement to the expected spectrum, the average percent errors increase to 2.6% and 5.5%, respectively. The increase in the percent error is mostly due to the non-negligible intensity gradient within the region. Spatial areas are defined such that the region size becomes comparable

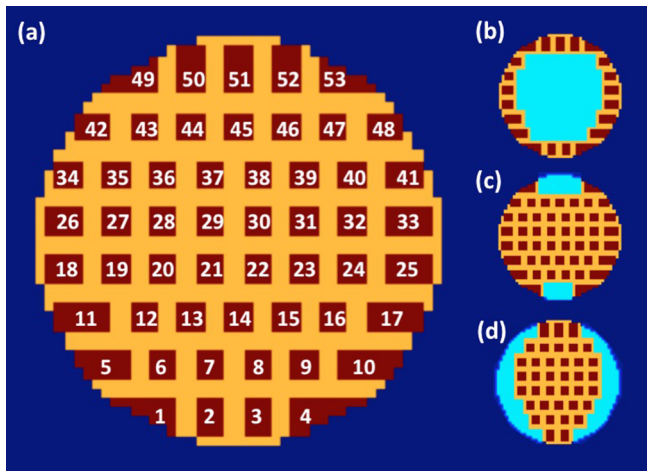

FIG. 4. (a) Rectangular spatial regions defined with spatial resolution, $\Delta x \sim$ 11 μm. (b)–(d) define the central region, top/bottom periphery, and left/right periphery, respectively, which have slightly different sources of discrepancies.

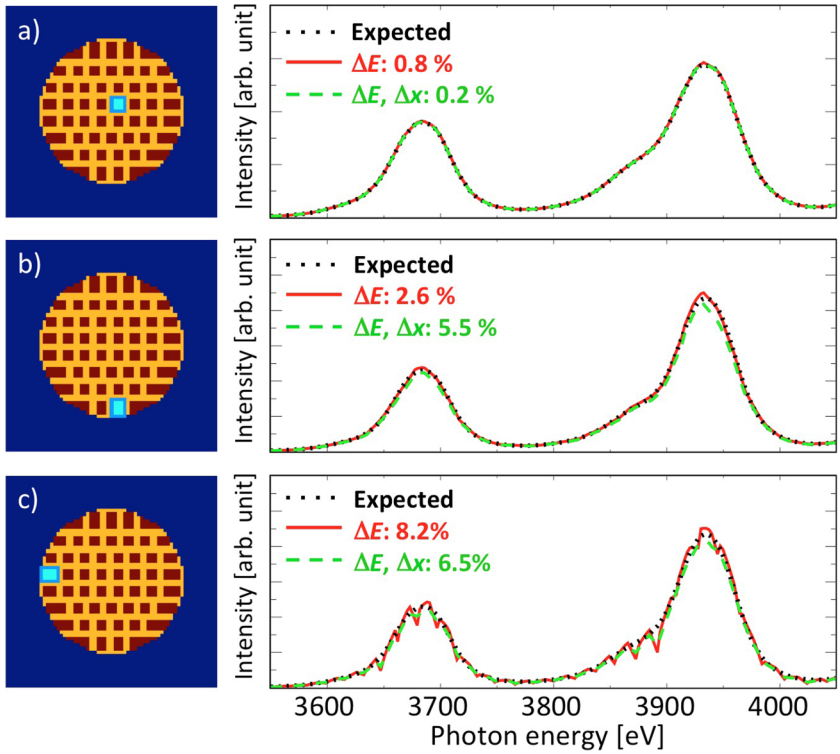

FIG. 5. 2-D space-resolved spectra extracted from synthetic MMI with (solid red) spectral-resolution effects only, and (dashed green) both spectral and spatial resolutions for (a) the central region, (b) the bottom periphery, and (c) the left periphery. The percentages shown are the average absolute percent errors with respect to the expected space-resolved spectra (dotted black).

to the spatial resolution so that the intensity variation over the region becomes negligible. However, image intensity always drops rapidly towards the image periphery, and negligible variations cannot be assumed for the peripheral regions. Thus, comparison between expected and reconstructed spectra from the peripheral regions is in general not as good as those for central regions.

Spectra extracted from the periphery have other issues when finite spatial resolution is taken into account (i.e., dashed green line). Finite spatial resolution smooths out the structure, and some signals are mixed in from the adjacent regions. Thus, at the periphery, spatial-resolution effects lower the overall intensity very slightly, but systematically, because the convolving area partially exceeds the object boundary. Since the spectral-resolution size is ~11 μm and small compared to the object size, these effects are subtle but still persist as observed in Fig. 3(b). In the case of image comparison, the systematic intensity drop at the periphery disappears by applying the point-spread function directly to the expected images. However, it is not as easy to take into account spatial-resolution effects in the space-resolved spectra modeling. Here, we do not introduce any correction associated with the edge effects but just summarize what we learn from the comparisons. Fortunately, their effects are small and systematic over the entire spectral range. This preserves the line ratios and widths, and thus these effects on the T_e and n_e analysis can be considered negligible.

Fig. 5(c) shows similar comparisons for a left/right-periphery region (i.e., region 26). One can observe that all the extracted space-resolved spectra show periodic structure about the expected spectrum, which results in increasing the percent errors to 8.2% and 6.5%, respectively. This periodic structure is observed in all space-resolved spectra extracted from the left/right-periphery regions.

These periodic structures originate from the non-negligible horizontal intensity gradient in the spatial region. For left/right-periphery regions, the intrinsic radial intensity gradients become horizontal, which is a problem because the horizontal axis is also the spectral axis. Figs. 6(a) and 6(b) show a blow-up of the partial MMI data associated with region 26 over the Ly-β region and the extracted spectrum, respectively. Each spatial region of Fig. 6(a) is slightly enlarged, and outside of region 26 is whitened out for communication purposes. Every region 26 of the synthetic MMI data shows horizontal intensity gradients monotonically increasing from left to right. Since each partial image is responsible for a different sub-range of the spectrum, the extracted spectrum inherits the periodic horizontal gradient structure. While we apply a first-order correction to this using the technique discussed in Sec. V of Ref. 9, the periodic structure is not perfectly removed.

Table I shows average percent errors computed for space-resolved spectra over each category defined in Figs. 4(b)–4(d). For the 32 central regions, extracted spectra are very accurate and show average percent error of less than 1%. Spectra extracted from the top/bottom periphery show larger discrepancies of 1.4% and 3.8%, respectively. The 1.4% is due to the non-negligible vertical intensity gradient. When the spatial-resolution effect is introduced, it slightly but systematically lowers the intensity, which results in increasing the percent error to 3.8%. For the left/right periphery, the percent errors become even larger—5.1% and 7.5%, respectively—due to

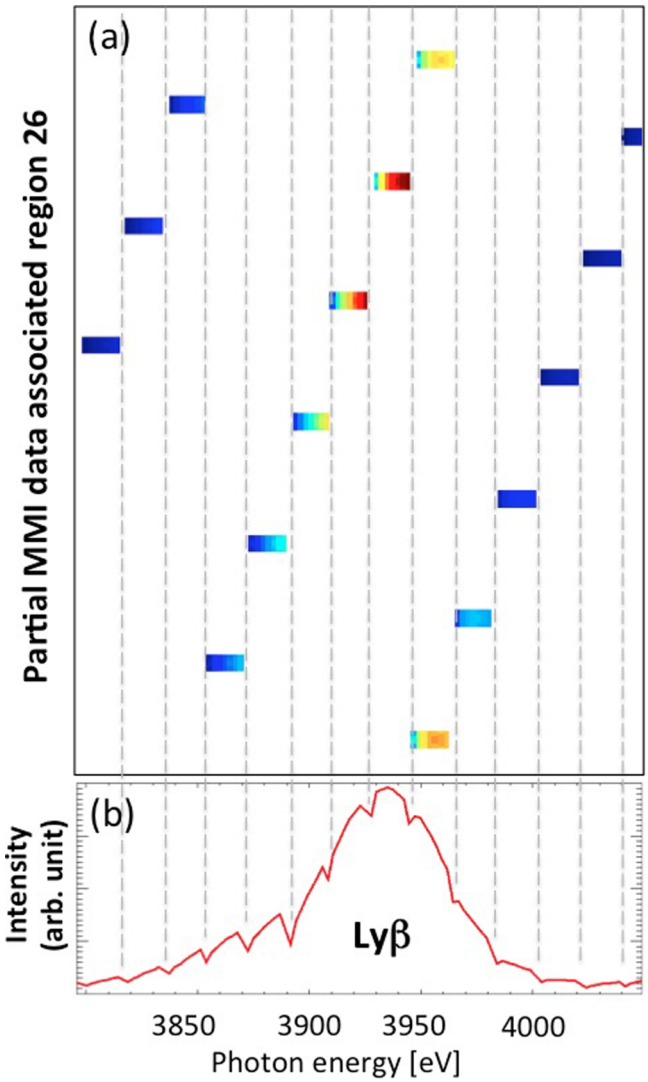

FIG. 6. (a) A left-periphery region (region 26) is picked out from each pinhole image of the MMI data and shown over the spectral range of Ly-β. (b) The spectra extracted from the partial MMI data show periodic structure originating from the repeating horizontal intensity gradient structures of the each rectangular region. The selected regions are slightly enlarged for display purposes.

the periodic structure originating from horizontal intensity gradients.

Table II shows the percent errors in inferred T_e and n_e and their standard deviations. Since we have both expected spectra and reconstructed spectra, we can investigate how the inaccuracies in the reconstructed spectra affect the inferred T_e

TABLE I. The percent errors averaged over the central, top/bottom-periphery, and left/right-periphery regions, respectively. The numbers of spectra are shown in parentheses. For peripheral regions, the percent error becomes larger when spatial-resolution effects are introduced. Left/right peripheral regions have larger errors than top/bottom peripheral region due to periodic structure introduced by the horizontal intensity gradients.

Intensity % error	ΔE (%)	$\Delta E, \Delta x$ (%)
Central (32)	0.6 ± 0.3	0.7 ± 0.4
Top/bottom periphery (5)	1.4 ± 0.3	3.8 ± 0.3
Left/right periphery (16)	5.1 ± 1.2	7.5 ± 1.9

TABLE II. The percent errors in T_e and n_e averaged over the central, top/bottom-periphery, and left/right-periphery regions, respectively. The errors are within a few percent.

T_e % error	ΔE (%)	$\Delta E, \Delta x$ (%)
Central (32)	0.0 ± 0.0	0.1 ± 0.1
Top/bottom periphery (5)	0.4 ± 0.5	0.5 ± 0.6
Left/right periphery (16)	0.7 ± 0.6	0.8 ± 0.7
n_e % error	ΔE (%)	$\Delta E, \Delta x$ (%)
Central (32)	0.2 ± 0.2	0.3 ± 0.3
Top/bottom periphery (5)	2.3 ± 1.1	3.1 ± 1.2
Left/right periphery (16)	1.8 ± 2.6	1.9 ± 2.1

and n_e. First, T_e and n_e are inferred from both expected spectra and reconstructed in the same way as described in Ref. 10. The percent errors in inferred T_e and n_e are computed for all 53 regions and averaged over central, top/bottom peripheral, and left/right peripheral regions. In spite of the noticeable discrepancies in reconstructed spectra shown in Fig. 5, they do not significantly affect the line ratios and widths and their impacts on the inferred conditions are all within a few percent.

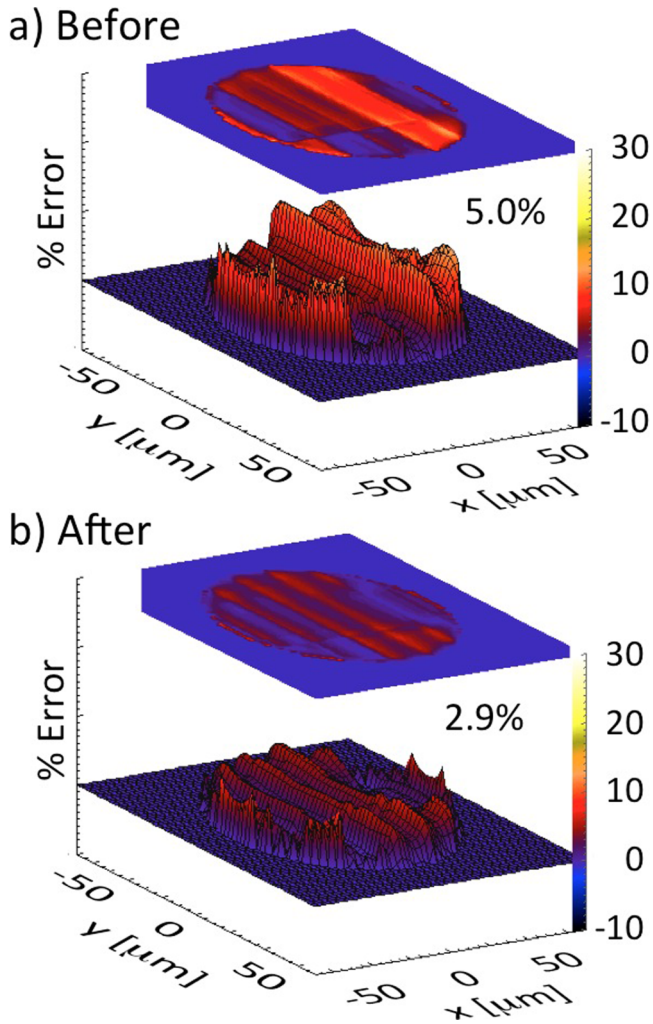

FIG. 7. Percent-error surface plots for reconstructed He-β images (a) before and (b) after applying the pinhole size-variation correction to the synthetic MMI data. Spatial-resolution effects are taken into account in the expected images.

To summarize, the dominant source of discrepancies for the peripheral regions is (i) systematic intensity lowering at the periphery due to spatial-resolution effects and (ii) the periodic structure due to horizontal intensity gradients.

IV. PINHOLE SIZE-VARIATION EFFECTS AND THEIR CORRECTION

Each pinhole of the pinhole array has a slightly different shape and size due to fabrication tolerance. As discussed in Sec. II C, pinhole size-variation introduces variation in brightness and in spatial resolution from one pinhole image to another. While the pinhole shape also affects the MMI data, its effect is neglected throughout this article. In this section, we simulate the impact of the pinhole size-variation effects on the reconstructed images and spectra. We then introduce a correction and discuss how well this correction removes the introduced bias from the reconstructed images and spectra. The uncertainty of the pinhole location is less than a few microns. This is much smaller than the spatial resolution of the instrument and thus not considered throughout this investigation.

First, we create synthetic MMI data with pinhole size-variation effects by following the technique discussed in Sec. II C. The pinhole size and its tolerance used in this synthetic study are 10 ± 1 μm, which are typical values for the pinhole array in our application. Both spectral resolution and spatial resolution are taken into account in the synthetic MMI data.

Fig. 7(a) shows the resultant percent-error surface plots for reconstructed Ar He-β images. The spatial-resolution effect is applied to the expected image used in the percent-error calculation as discussed in Sec. III A. Compared to Fig. 3(c), the overall error increases from 1.4% to 5.0%. More importantly, it introduces a bias in the spatial shape. There is a larger error band (~10%) along the y direction. We confirm that the signal of this bright region comes from a single pinhole image in the synthetic MMI data whose pinhole size is about 5% larger than the nominal and whose intensity is $B(D_p) = (1.05)^2 \approx 10\%$ brighter than the nominal.

The solid green lines in Fig. 8 are space-resolved spectra reconstructed from synthetic MMI data with pinhole size variations for (a) a central region, (b) a bottom peripheral region, and (c) a left peripheral region. Compared to the reconstructed spectra without pinhole size-variation effects in Fig. 5, the overall percent errors increase from (a) 0.2% to 8.8%, (b) 5.5% to 8.7%, and (c) 6.5% to 9.3%, respectively. For peripheral regions, one might think that the impact is not as large since the errors without pinhole size-variation effects are already showing ~6%. However, percent errors without pinhole size-variation effects are systematic without changing the line ratios and widths [i.e., the green lines in Fig. 5], while percent errors due to the pinhole size-variation effects could affect the line ratios and the widths. Thus, from a diagnostics point of view, the errors due to the pinhole size-variation effects are more important than those due to the systematic intensity lowering and periodic structure discussed in Sec. III B.

The introduced bias observed in this synthetic investigation is a concern for the actual MMI data analysis. For example, if one of the pinholes appearing at a line center happens to have a size larger than the vendor's tolerance, this could introduce significant spatial bias to the extracted images

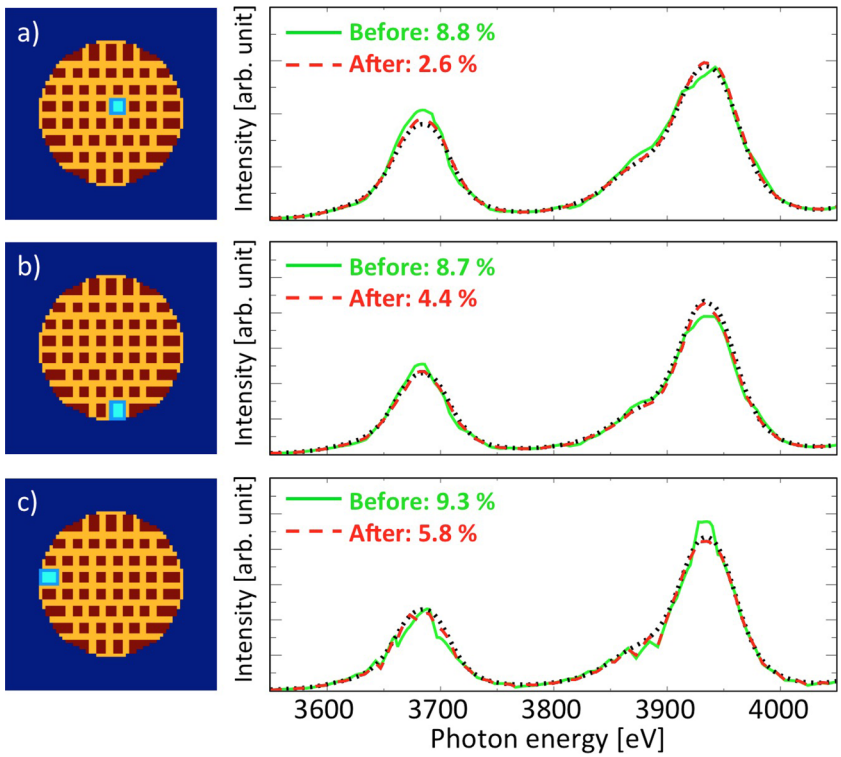

FIG. 8. Space-resolved spectra over the He-β and Ly-β spectral range (solid green) before and (dashed red) after the pinhole size-variation correction for (a) a central region, (b) a bottom peripheral region, and (c) a left peripheral region. The dotted black spectra are the expected spectra.

and spectra. One way to check the pinhole size variation would be to perform a preshot measurement of the pinhole-array transmission. However, since there are over a thousand pinholes in a pinhole array and only a fraction of those appears in each MCP strip, it remains a technical challenge to connect such preshot data to the actual MMI data. Here, we discuss a technique to extract the pinhole size variation directly from the data and test the technique in the synthetic MMI data to quantify its accuracy.

Each pinhole size would affect each image of MMI data in two ways: (1) spatial resolution and (2) brightness. Of these two effects, the dominant effect is brightness variation from one image to another because brightness is proportional to the square of the diameter and thus 10% error in diameter results in 21% in brightness. Fig. 9(a) shows synthetic MMI data containing 10%-pinhole-size-variation effects used to reconstruct the images and spectra shown in Figs. 7 and 8. It is not clear which pinhole images are brighter or dimmer from the MMI data due to the horizontal spectral features on the MMI data. However, these spectral features can be roughly removed by simply dividing each row of the MMI data by the space-integrated spectrum.[9]

Fig. 9(b) shows synthetic MMI data with spectral features removed. It is now clearer which pinhole images are brighter or dimmer. Since we are interested in the overall brightness of each pinhole image, we integrate intensity values within each pinhole image and display each image according to its space-integrated intensity. Fig. 9(c) shows the resultant brightness-variation image. The brightness variation in the MMI data can be suppressed by dividing the MMI image [i.e., 9(a)] by this extracted brightness-variation image pixel by pixel.

Fig. 10(a) shows the original brightness variation used to create Fig. 9(a) and is very similar to the derived one, Fig. 9(c). We can quantify the accuracy of the derived brightness variation by dividing Fig. 10(a) by Fig. 9(c) pixel by pixel. The resultant image in Fig. 10(b) shows not only the accuracy of the derived brightness variation but also how well this technique can remove the brightness variation from the MMI data. We confirm that this technique successfully reduces the brightness variation from 8% to 3%. The relative pinhole size variation can also be computed from the derived relative brightness by $D_p/D_{PH} = \sqrt{B}$ and compared with the used one. We find the average percent error in the derived relative pinhole size is 2% ± 2%.

To quantitatively investigate the impact of the brightness-variation correction on the reconstructed images and spectra, the correction is applied to the synthetic MMI data [i.e., Fig. 9(a)]. Then, the percent-error surface plot for the He-β image is re-computed, and the space-resolved spectra are reconstructed for comparison.

Fig. 7(b) shows the percent-error surface plot for He-β after the brightness-variation correction. The average error is reduced from 5.0% to 2.9%. More importantly, the spatial

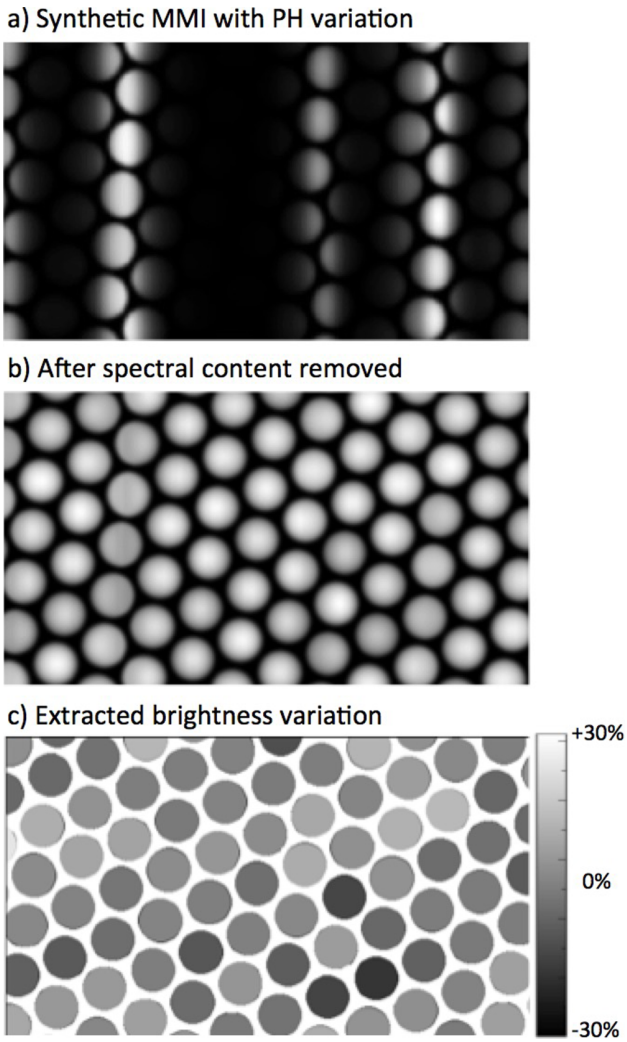

FIG. 9. (a) Synthetic MMI data with pinhole size-variation effects ($\Delta D/D = 0.1$). (b) Spectral content is removed from (a). (c) Overall brightness of each pinhole is computed by integrating the intensity within each pinhole image and replacing the pixel values with this integration. We observed that the brightness is indeed slightly different for each pinhole image.

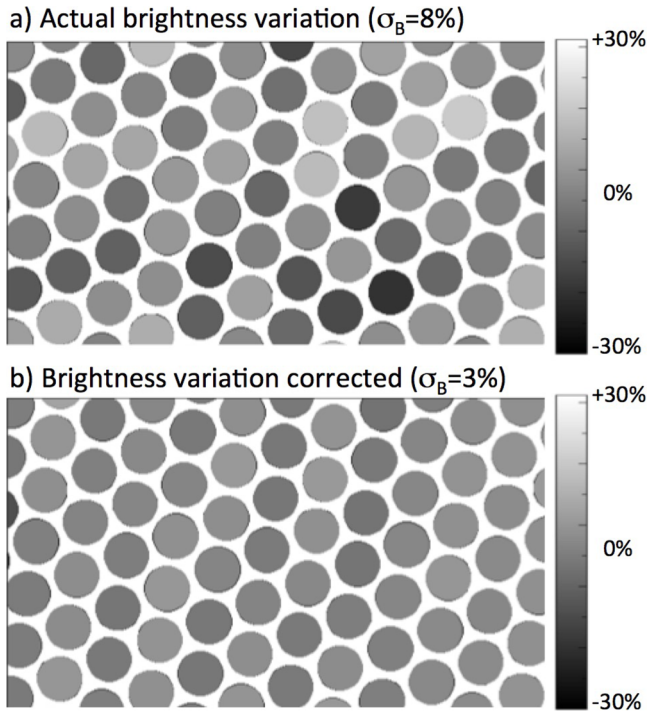

FIG. 10. (a) Original simulated brightness variations used to create Fig. 9(a). (b) Brightness variation after the correction is applied.

TABLE III. Average and standard deviation of the space-resolved spectra percent errors over the 32 central regions and over the 21 peripheral regions before and after the brightness-variation correction.

Intensity % error	Before (%)	After (%)
Central (32)	5.3 ± 0.3	1.5 ± 0.1
Top/bottom periphery (5)	5.3 ± 0.4	3.1 ± 0.3
Left/right periphery (16)	7.8 ± 1.2	7.0 ± 1.8

TABLE IV. The percent errors in T_e and n_e averaged over the central, top/bottom-periphery, and left/right-periphery regions, respectively. The errors decrease after the pinhole size-variation correction.

T_e % error	Before (%)	After (%)
Central (32)	2.1 ± 1.0	0.3 ± 0.2
Top/bottom periphery (5)	2.4 ± 1.3	1.0 ± 1.1
Left/right periphery (16)	1.2 ± 1.3	0.8 ± 0.6
n_e % error	Before (%)	After (%)
Central (32)	2.8 ± 2.0	2.0 ± 1.0
Top/bottom periphery (5)	3.1 ± 2.8	2.3 ± 1.7
Left/right periphery (16)	5.7 ± 4.5	1.7 ± 2.4

bias due to the pinhole size variation [i.e., large error band in Fig. 7(a)] is significantly reduced.

The dashed red curves in Fig. 8 show the space-resolved spectra reconstructed from synthetic MMI data after the correction. The average percent error is reduced (a) from 8.8% to 2.6%, (b) from 8.7% to 4.4%, and (c) from 9.3% to 5.8%, respectively. One can visually confirm that the correction successfully removes the bias associated with the brightness variation and significantly improves the space-resolved spectra.

The same analysis is repeated for all the spectra, and the percent errors are summarized for each category in Table III. The average errors for the space-resolved spectra reconstructed for each category are lowered from 5.3% to 1.5% for central regions, 5.3% to 3.1% for top/bottom peripheral regions, and 7.8% to 7.0% for left/right peripheral regions. For the peripheral regions, the average error is still high because the main source of error is the systematic intensity lowering and the periodic oscillations. However, the bias introduced by the pinhole size-variation effects is successfully removed as shown in Figs. 8(b) and 8(c). The conditions inferred from the corrected spectra are accurate to less than a few percent errors (Table IV).

V. DISCUSSION AND SUMMARY

While the MMI instrument is a powerful diagnostic tool to constrain spatial structure of inertial confinement fusion plasmas, the reliability of the reconstructed images and spectra has not been investigated before. Due to the discrete nature of MMI data, the accuracy of the reconstructed images and spectra is somewhat limited. In this article, we synthetically investigated and quantified the accuracy of the images and spectra reconstructed from synthetic MMI data for the application to OMEGA direct-drive Ar-doped D_2 ICF implosion experiments.

The intensities of the reconstructed images are accurate to less than a few percent error as long as spatial effects are taken into account. The reconstructed space-resolved spectra are accurate for central regions of the core image. The intensities of the space-resolved spectra reconstructed for the peripheral regions are slightly but systematically lowered due to the MMI spatial-resolution effects on the spectra. This increases the percent error to 3%–4%. We note that the exact effects on the periphery are more complicated because the boundary motion is integrated over a finite detector duration. Also, the plasma boundary itself becomes elusive. Especially, for ICF plasmas, there is fuel-shell mixing due to hydrodynamic instabilities. These are very important aspects but beyond the scope of this article. For left/right peripheral regions, the reconstructed spectra inherit intrinsic horizontal intensity gradients, which result in periodic structure in the spectra. This increases the percent error to ~7%. Fortunately, these systematic intensity-lowering and periodic structures do not change line ratios and widths significantly, and their impact on the plasma condition diagnostics is less than a few percent.

One potential source of bias in the reconstructed images and spectra is that due to pinhole size-variation effects. The simulation shows this is small (i.e., ~5%). However, we confirmed that it can introduce ~10% spatial bias in the reconstructed images and ~10% change in the line ratios in the spectra. Since some pinholes could have a larger/smaller size beyond the vendor's specification, it has to be somehow measured and corrected. We developed a technique to extract its dominant effect, i.e., brightness variation. The images and spectra reconstructed from the corrected MMI data successfully remove the bias introduced by the pinhole size variations. The conditions inferred from the corrected MMI data are accurate to less than a few percent errors.

These investigations provide a better understanding for the successful use of MMI diagnostics and the reliability and limitations of the reconstructed images and spectra for OMEGA direct-drive ICF Ar-doped D_2 implosion experiments. While the MMI data reliability for other applications are beyond the scope of this article, the reliability depends on the criterion discussed in Ref. 13, which depends on the object size, MCP strip width, pinhole-array design, magnification, and line spectral width. Thus, as long as the MMI setup is similar, the object size is comparable, and the electron density is similar, the reliability of the images and spectra would be quantitatively similar to those discussed in this article.

MMI diagnostics are unique and constrain the object spatial information with unprecedented level of detail. However, the complexity of MMI data should not be underestimated. Ideally, it is important to perform similar synthetic investigations for individual applications because the impact of each investigated issue could differ per application.

ACKNOWLEDGMENTS

This work was supported by DOE/NLUF Grant Nos. DE-NA0000859 and DE-NA0002267, and LLNL. T. Nagayama

thanks R. E. Falcon for his help in refining the manuscript. R. Florido thanks support from EUROfusion ToIFE project.

[1]J. Nuckolls, L. Wood, A. Thiessen, and G. Zimmerman, Nature **239**, 139 (1972).
[2]J. D. Lindl, P. Amendt, R. L. Berger, S. G. Glendinning, S. H. Glenzer, S. W. Haan, R. L. Kauffman, O. L. Landen, and L. J. Suter, Phys. Plasmas **11**, 339 (2004).
[3]J. Lindl, O. Landen, J. Edwards, E. Moses, and N. Team, Phys. Plasmas **21**, 020501 (2014).
[4]D. S. Clark, M. M. Marinak, C. R. Weber, D. C. Eder, S. W. Haan, B. A. Hammel, D. E. Hinkel, O. S. Jones, J. L. Milovich, P. K. Patel, H. F. Robey, J. D. Salmonson, S. M. Sepke, and C. A. Thomas, Phys. Plasmas **22**, 022703 (2015).
[5]J. A. Koch, T. W. Barbee, N. Izumi, R. Tommasini, R. C. Mancini, L. A. Welser, and F. J. Marshall, Rev. Sci. Instrum. **76**, 073708 (2005).
[6]R. Tommasini, J. A. Koch, N. Izumi, L. A. Welser, R. C. Mancini, J. Delettrez, S. Regan, and V. Smalyuk, Rev. Sci. Instrum. **77**, 10E303 (2006).
[7]L. A. Welser, R. C. Mancini, J. A. Koch, S. Dalhed, R. W. Lee, I. E. Golovkin, F. Marshall, J. Delettrez, and L. Klein, Rev. Sci. Instrum. **74**, 1951 (2003).
[8]N. Izumi, T. W. Barbee, J. A. Koch, R. C. Mancini, and L. A. Welser, Rev. Sci. Instrum. **77**, 083504 (2006).
[9]T. Nagayama, R. C. Mancini, R. Florido, R. Tommasini, J. A. Koch, J. A. Delettrez, S. P. Regan, and V. A. Smalyuk, J. Appl. Phys. **109**, 093303 (2011).
[10]T. Nagayama, R. C. Mancini, R. Florido, D. Mayes, R. Tommasini, J. A. Koch, J. A. Delettrez, S. P. Regan, and V. A. Smalyuk, Phys. Plasmas **21**, 050702 (2014).
[11]T. Nagayama, R. C. Mancini, R. Florido, R. Tommasini, J. A. Koch, J. A. Delettrez, S. P. Regan, V. A. Smalyuk, L. A. Welser-Sherrill, and I. E. Golovkin, Rev. Sci. Instrum. **79**, 10E921 (2008).
[12]T. Nagayama, R. C. Mancini, R. Florido, D. Mayes, R. Tommasini, J. A. Koch, J. A. Delettrez, S. P. Regan, and V. A. Smalyuk, Phys. Plasmas **19**, 082705 (2012).
[13]T. Nagayama, R. C. Mancini, D. Mayes, R. Tommasini, and R. Florido, High Power Laser Sci. Eng. **3**, e23 (2015).
[14]M. F. Gu, Can. J. Phys. **86**, 675 (2008).
[15]R. Florido, R. Rodríguez, J. M. Gil, J. G. Rubiano, P. Martel, E. Mínguez, and R. C. Mancini, Phys. Rev. E **80**, 56402 (2009).
[16]J. C. Stewart and K. D. J. Pyatt, Astrophys. J. **144**, 1203 (1966).
[17]R. C. Mancini, R. F. Joyce, and C. F. Hooper, Jr., J. Phys. B: At. Mol. Phys. **20**, 2975 (1987).
[18]R. C. Mancini, D. P. Kilcrease, L. A. Woltz, and C. F. Hooper, Jr., Comput. Phys. Commun. **63**, 314 (1991).
[19]D. Mihalas, *Stellar Atmospheres*, Astronomy and Astrophysics Series (W. H. Freeman, 1978).